

Article

Phosphorus Species in Deep-Sea Carbonate Deposits: Implications for Phosphorus Cycling in Cold Seep Environments

Junlie Zhou ^{1,2}, Mengran Du ¹, Jiwei Li ¹, Hengchao Xu ¹, Kaiwen Ta ^{1,3}, Shun Chen ¹ and Xiaotong Peng ^{1,*}

¹ Laboratory of Deep-Sea Geology and Geochemistry, Institute of Deep-Sea Science and Engineering, Chinese Academy of Sciences, Sanya 572000, China; zhoujl@idsse.ac.cn (J.Z.); mdu@idsse.ac.cn (M.D.);

lijjwei20025@idsse.ac.cn (J.L.); hcxu@idsse.ac.cn (H.X.); takaiwen@idsse.ac.cn (K.T.); chans@idsse.ac.cn (S.C.)

² University of Chinese Academy of Sciences, Chinese Academy of Sciences, Beijing 100049, China

³ Southern Marine Science and Engineering Guangdong Laboratory (Zhuhai), Zhuhai 519000, China

* Correspondence: xtpeng@idsse.ac.cn; Tel.: +86-898-8838-0172

Received: 17 June 2020; Accepted: 21 July 2020; Published: 21 July 2020



Abstract: Phosphorus (P) is an important nutrient for biological communities in cold seeps. However, our knowledge on the source, species, and cycling of P in cold seep environments is limited. In this study, the concentration, species, and micro to nanometer scale distribution of P in seep carbonates were examined at three deep-sea cold seeps in the South China Sea and East China Sea. The Ca-P accounts for the largest proportion of P—followed by detrital-P, Fe-P, organic-P, and exchangeable-P. The distribution patterns of Ca-P, detrital-P, and organic-P in the seep carbonates differ from one another, as shown by elemental mapping with NanoSIMS and scanning electron microscopy. The covariation of P with Ca and C reveals that Ca-P co-precipitates with Ca-carbonate, which is linked to the process of sulfate-driven anaerobic oxidation of methane. Organic-P is also observed within biofilm-like organic carbon aggregates, revealing the microbial enrichment of P by fluids in the process of anaerobic oxidation of methane. P with a granulated morphology was identified as detrital-P derived from deep sediments. Most importantly, it is evident that Ca-P is positively correlated to the Fe content in all the seep carbonates. This indicates the likelihood that the dissolved P in cold-seep fluids is released primarily from Fe oxides through Fe-driven anaerobic oxidation of methane in deep sediments. These processes associated with different species of P may have significant implications for P geochemical cycling and anaerobic oxidation of methane impelled by Fe and sulfate reduction in cold seep environments.

Keywords: seep carbonates; phosphorus species; phosphorus cycling; anaerobic oxidation of methane; cold seep environments

1. Introduction

Phosphorus, an important nutrient that controls primary productivity [1,2], is cycled throughout various environments. All organisms require P in addition to C, energy sources, and electron acceptors and donors to synthesize nucleic acids, fatty acids, and for energy reactions. This includes those communities of organisms that are found around cold seeps, which are among the most widespread chemosynthesis-based ecosystems in the deep-sea [3]. Animals and microorganisms found around cold seeps can use dissolved inorganic PO_4^{3-} in cold-seep fluids and/or seawater and dissolved organic PO_4^{3-} compounds produced by the cold seep communities themselves. For example, sulfate reducing bacteria, partners of anaerobic oxidation of methane consortia [4], can accumulate significant amounts of P in their cells during the anaerobic oxidation of methane [5].

Previous studies have revealed that carbonates from various cold seep environments contain a variety of P precipitates [6–11]. This indicates that P is commonly enriched in cold seep fluids. The composition of carbonate deposits recovered from the northern Okinawa Trough in the East China Sea is, for example, characterized by up to 12.6% P in the form P_2O_5 [12]. High P concentrations are accompanied by high Fe concentrations, particularly in carbonate samples recovered from the Congo deep-sea fan [7] and the Gulf of Cadiz [6]. This implies that there may be an intrinsic link between the P and Fe. The latter is a species involved in Fe-driven anaerobic oxidation of methane and Fe reduction coupled to oxidation of organic matter [1,12,13]. Although several studies of the biogeochemistry of C, N, and S have been carried out at cold seeps [14–18], our knowledge of the geochemical cycling of P in similar systems is limited. Data on the species, source, and fate of P in submarine cold seep environments is sparse.

During the past decade, ~40 cold seeps have been discovered in the South China Sea and East China Sea [3,14,19]. Our study sites in the South China Sea (Site F and Haima) are the only two known active cold seep fields on the northern slope of the South China Sea [20,21]. Site E in the East China Sea is an inactive cold seep field on the slope of the northern Okinawa Trough [12,22,23]. These sites allow comparison of the difference in composition of P between the low P (Haima and Site F) and high P (Site E) cold seep systems. The goals of this study are to (1) obtain the composition of P in cold seep carbonates, (2) identify different P species in cold seep carbonates, and (3) elucidate the source and fate of P and its potential linkage with anaerobic oxidation of methane. This study provides fresh insights into P geochemical cycling in deep-sea cold seep environments.

2. Geological Setting and Sampling

The Haima cold seeps are found at a depth of 1370–1390 m in the southern part of the Qiongdongnan Basin, which is located in the northwestern South China Sea (Figure 1). The Red River strike-slip fault marks the western boundary of the Qiongdongnan Basin, where bottom simulating reflectors and gas chimneys have been widely identified. The Haima cold seeps were first discovered in 2015 during the cruise of the research vessel *Haiyang-6* with Remote Operated Vehicle (ROV) *Haima*. Six cold seeps were identified in this area during the joint cruise of the ROV *Haima* and Human Occupied Vehicle (HOV) *Shenhaiyongshi* in June 2018. Gas hydrates were observed at the margins of the vent during the HOV dives and were also recovered in subsurface sediments at approximately 4 m below the seafloor using gravity core [20] (Figure S1B).

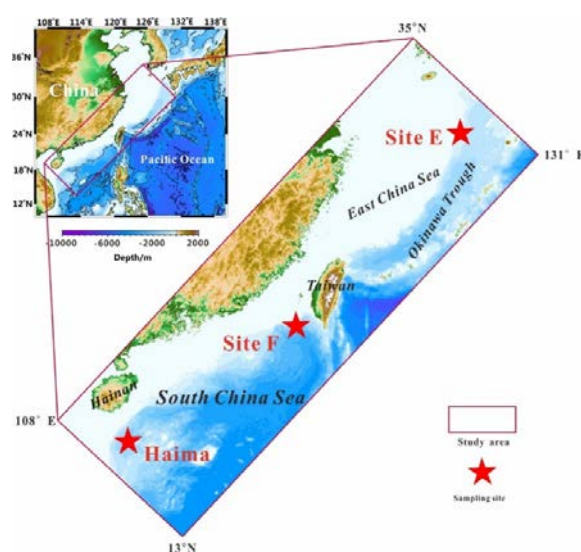


Figure 1. Location of three sampling sites (red star) in the northern South China Sea and in the East China Sea.

The cold seeps at Site F, which is located on the Formosa Ridge on the northeastern continental slope of the South China Sea, are located in water that is 1120 m deep (Figure 1). The Formosa Ridge is an NNW–SSE oriented ridge that is nearly 2 km long and rises over 100 m above the surrounding seabed. An active gas plume on top of the ridge, first identified in 2008, was inferred to be generated by active methane seepage [21]. Initial surveys of the surrounding area by the HOV *Jiaolong* in 2013 indicated that the field extends approximately 50 × 100 m and hosts several active seeps. Mussels and crabs, which are common seep-associated consumers, dominate this cold seep field. The ridge crest is characterized by large cold-seep carbonate blocks and pavements [14] (Figure S1C).

The inactive cold seep field in the East China Sea (named Site E herein) lies at the head of a small-scale submarine canyon that incises the western slope of the northern Okinawa Trough at a water depth of ~630 m (Figure 1). The Okinawa Trough, which is a back-arc basin formed by extension in the continental lithosphere behind the Ryukyu trench-arc system, has a typical U shape [24]. The high sedimentary supply probably comes from the river systems that are adjacent to the East China Sea continental shelf, such as the Yangtze River and the Yellow River [25]. Topographically, submarine canyons, fans, and turbidite deposits are extensively developed on the western slope of the northern Okinawa Trough. A bottom-simulating reflection in the area around Site E, identified by a high-resolution multi-channel seismic survey, indicates that there may be a natural gas hydrate reservoir beneath the sea floor [23]. Several carbonate chimneys, crusts, concretions, mollusk shells, and other animals are present at Site E [23] (Figure S1A).

In this study, 8 carbonate samples from the Haima cold seeps and 8 carbonate samples from the Site F cold seeps were collected from different dives in June 2018 using manipulators installed on HOV *Shenhaiyongshi*, during the cruise of R/V *Tansuoyihao*, which investigated the cold seeps in the northern SCS. Meanwhile, 13 carbonate samples from the Site E were recovered using geological dredges during the integrated environmental and geological expedition of R/V *KexueYihao* in July–August 2013. All the samples used in this study came from the seep carbonates on the seafloor: They are not fragments from the sediment surface. Once on board, the carbonate samples were subsampled and stored at −20 °C for further geochemical analysis. After freeze drying, sub-samples from the seep carbonates that did not contain organisms were selected and powdered for geochemical analyses. A rock saw was used to obtain subsamples for light microscopy, Raman spectroscopy, scanning electron microscopy, and NanoSIMS analyses.

3. Methods

3.1. Light Microscopy

Subsamples were impregnated with a polyester resin mix under vacuum and polished thin sections were prepared (30 mm × 50 mm surface area, 30 μm thickness). A Leica DM2700P polarizing light microscope was used to analyze polished thin sections of carbonate rocks and ascertain areas for in-situ analysis on the surfaces of freshly fractured carbonate rocks in transmitted and reflected light in the Laboratory of Deep-sea Geology and Geochemistry at the Institute of Deep-sea Science and Engineering, Chinese Academy of Sciences.

3.2. X-ray Diffraction (XRD)

XRD analyses were performed on a D8 Advance X-ray diffractometer (Bruker) at 40 kV and 30 mA with CuK-alpha radiation (1.54061 Å) and a graphite monochromator at the Guangzhou Institute of Geochemistry, Chinese Academy of Sciences. Sample mounts were step-scanned from 3° to 85° (2θ) with a step-size of 0.02° and counting time of 50 s. Semi-quantitative phase analyses were performed on a PDF22004 computer with Jade 6.5 software.

3.3. Major and Trace Element Analyses

The major elements were measured by X-ray fluorescence using a Shimadzu XRF-1800 spectrometer at 40 kV and 95 mA at State Key Laboratory of Marine Geology, Tongji University. Ten major elements were analyzed quantitatively after fusing 0.8 g of sample material with 8.0 g of dilithium tetraborate at 1050 °C for ~16 min. The samples were dissolved in a solution of HNO₃ + HF on a hot plate. The eluted sample was diluted by 2% HNO₃ for the trace element measurement by using Inductively Coupled Plasma Mass Spectrometer (ThermoFisher VG-X7) at State Key Laboratory of Marine Geology, Tongji University. The precision of the sample duplicates as well as of the repeated analyses was ~3%.

3.4. Sequential P Extraction

Sedimentary P species were determined by the sequential extraction method developed and revised for marine sediments [26,27]. Samples of ground rock (100 mg) were used for sequential extraction of P. The exchangeable P was determined as MgCl₂ (1 mol·L⁻¹, pH = 8, 0.5 h, 20 °C). Fe-bound P was determined as citrate-dithionite bicarbonate (CDB, pH = 7.3, 8 h, 20 °C) extractable P and treated with a 1 M MgCl₂ (pH = 8, 0.5 h, 20 °C) wash solution. The sediment residue was subsequently extracted with 1 M Na-acetate buffer (pH = 4, 6 h, 20 °C) and treated with a 1 M MgCl₂ (pH = 8, 0.5 h, 20 °C) wash solution to determine authigenic Ca-P. Detrital P was determined as 1 M HCl extractable P (24 h). Organic-P was determined non-sequentially as the difference between 1 M HCl extractable P (24 h) before and after ignition of the sediment (550 °C, 2 h). The P extractions were performed under oxygen-free conditions to prevent artifacts owing to sample oxidation [28]. The P concentrations in all the extracts except the buffered citrate-dithionite extracts were measured using the molybdenum blue colorimetric method [29]. The citrate-dithionite extracts were analyzed for Fe and P by using an inductively coupled plasma optical emission spectrometer (ThermoFisher IRIS Advantage) with a precision of ~0.5% at State Key Laboratory of Marine Geology, Tongji University.

3.5. Raman Spectroscopy and Imagery

Raman experiments were conducted in the Laboratory of Deep-sea Geology and Geochemistry at the Institute of Deep-sea Science and Engineering, Chinese Academy of Sciences. A WiTec alpha300 Rconfocal Raman imaging system equipped with a 532 nm Nd:YAG laser, spectrometer with a CCD camera (Peltier cooled to ~60 °C), and 50× objective (NA = 0.75) was used in our experiments. To prevent spectral artifacts caused by polishing, the laser beam was focused on carbonaceous microfossils beneath the surface of polished thin sections [30]. The laser power on the sample surface was maintained between 0.2 and 1 mW measured at the objective to prevent thermal alteration of the samples. After locating a region of interest in the field of view of the microscope, 2D Raman intensity maps of the surface were collected from predefined areas with a spatial resolution of 1 μm, and a full Raman spectrum was collected at each pixel in the measured area with an integration time of ~15 s. To remove the fluorescence background, a linear baseline was subtracted from each spectrum in the range of 200–1800 cm⁻¹.

3.6. Scanning Electron Microscopy and Element Mapping

Minerals and carbonaceous matters at the surface of the polished thin sections and freshly fractured carbonate rocks were examined with a ThermoScientific Apreo C scanning electron microscope that is equipped with an Energy-dispersive X-ray spectroscopy and AZtec system provided by Oxford Instruments, in the Laboratory of Deep-sea Geology and Geochemistry at the Institute of Deep-sea Science and Engineering, Chinese Academy of Sciences. The scanning electron microscopy was operated at 2 kV with a working distance of 10 mm to provide optimal imaging and to minimize charging and sample damage in the backscattered electron imaging mode. An accelerating voltage of 20 kV was used for the X-ray analysis to obtain adequate X-ray counts with a precision of ~5%.

3.7. NanoSIMS Ion Mapping

NanoSIMS elemental mapping was performed on the polished thin sections and freshly fractured carbonate rocks by using a Cameca NanoSIMS 50L (Cameca, Paris, France), at the Institute of Geology and Geophysics, Beijing, Chinese Academy of Sciences. The NanoSIMS is capable of imaging at a sub-50 nm lateral resolution for negatively charged secondary ions. To remove the conductive coating (Au) and the contaminants that were generated during pretreatment, each region of interest was pre-sputtered with a 150 pA beam current and an ion dose of $N = 5 \times 10^{16}$ ions/cm² [31]. In the multi-collection mode, negative secondary ions (¹²C⁻, ¹²C¹⁴N⁻, ³¹P⁻, ³²S⁻, and ⁴⁰Ca¹⁶O) were sputtered from the sample surface using a Cs⁺ primary beam with an intensity of ~2.5 pA and detected in a multi-collection mode.

4. Results

4.1. Mineralogy and Geochemistry of the Carbonates

XRD diffractograms (Figure S2) reveal that the carbonate deposits from Site E in the East China Sea are composed mainly of quartz, K-feldspar, and calcite, whereas those from Site F and Haima have aragonite as the dominant constituent and small amounts of quartz. The high content of detrital minerals at Site E (e.g., quartz and feldspar) reflects an abundant sedimentary supply from the East China Sea continental shelf [12]. These results are consistent with the analysis of major chemical composition (Table S1) that show that the carbonate deposits from Site E have high SiO₂ (38.8–55.8%), Al₂O₃ (6.6–10.3%), and CaO (12.5–19.9%) contents, whereas those from the SCS are characterized by higher CaO content (42.8–47.9% and 19.9–47.3% at Haima and Site F, respectively) and lower SiO₂ content (5.4–12.2% and 7.9–36.0% at Haima and Site F, respectively). The Fe₂O₃ content is higher in the carbonate deposits from Site E (2.6–7.7%) and Site F (0.6–0.80%) than in those from Haima (0.5–2.4%). The P₂O₅ content exhibits a distinct difference among the three sites, with higher values at site E (8.0–9.2%), followed by site F (0.07–2.3%) and Haima (0.05–0.08%).

4.2. P species Determined by Sequential P Extraction

The total sedimentary P concentrations obtained by the sequential extraction method match well with the P₂O₅ content determined by XRF, with a correlation coefficient of 0.9848 (Figure S3). This reveals the efficient P recovery by the sequential extraction procedures in carbonate rocks.

The total sedimentary P concentrations (24.36–1509.59 μmol-P/g) of the carbonates from Site E in the East China Sea are higher than those from Site F (16.13–123.74 μmol-P/g) and Haima (9.86–13.23 μmol-P/g) in the South China Sea (Figure 2, Table S2). The concentrations of the total inorganic P are in the ranges 23.78–1497.73 μmol-P/g, 13.57–122.13 μmol-P/g, and 9.27–12.64 μmol-P/g at Site E, Site F, and Haima, respectively. Meanwhile, the total organic phosphorus concentrations vary within 0.6–16 μmol-P/g, 0.70–1.6 μmol-P/g, and 0.6–0.8 μmol-P/g at Site E, Site F, and Haima, respectively. As with total sedimentary P, total inorganic P, and total organic P, the concentrations of Ca-P and detrital-P in the carbonates from Site E are also apparently higher than those from Site F and Haima.

Although the concentrations of the various P species are distinctly different among the three sites, the partitioning of P species in all the carbonate deposits exhibits a similar trend (Figure 2). Total inorganic P is the predominant form of total sedimentary P, constituting 93–99%. Organic-P, however, occupies a marginal fraction of the total sedimentary P (1–7%). Within the total inorganic P, Ca-P (21–77%) accounts for the largest proportion, followed by detrital-P (4–50%) or iron-bound P (Fe-P) (1–59%). Exchangeable-P (1–15%) accounts for the smallest fraction of the total inorganic P.

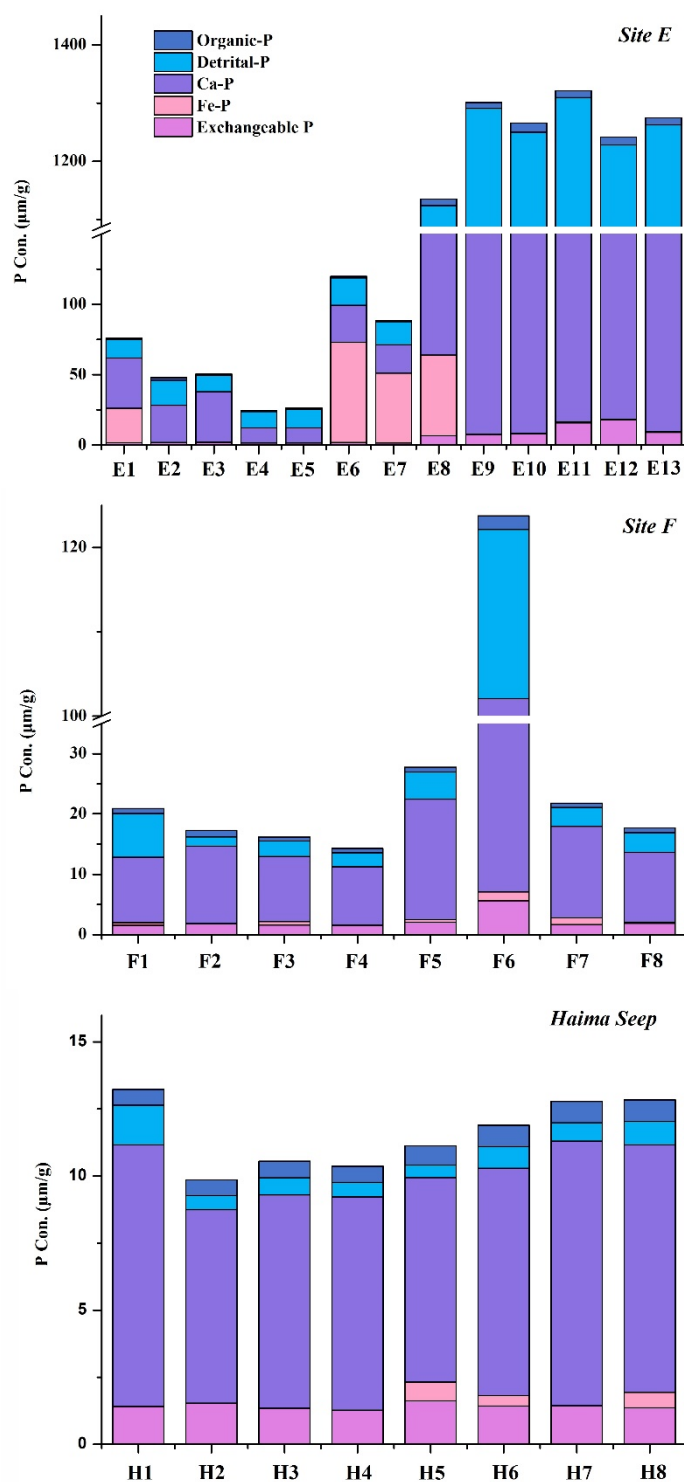


Figure 2. Concentrations of P among five different sedimentary species from samples of three cold seep sites. Total sedimentary P concentrations of samples from Site E are higher than samples from the other two sites. Ca-P is the main specie in cold seep carbonates at all three sites, following by detrital-P, Fe-P, exchangeable-P, and organic-P.

Positive correlations are evident between Ca-P and Fe_2O_3 in the carbonate deposits of Site F and Haima in the South China Sea (Figure 3), which are characterized by lower P contents. Positive correlations could be observed in the samples from Site E as well as the samples are divided into high

P ($P_2O_5 > 2.5\%$) and low P groups ($P_2O_5 < 2.5\%$) for comparison. However, Fe_2O_3 does not exhibit correlation with organic-P, detrital-P, exchangeable-P, or Fe-P at the three sites.

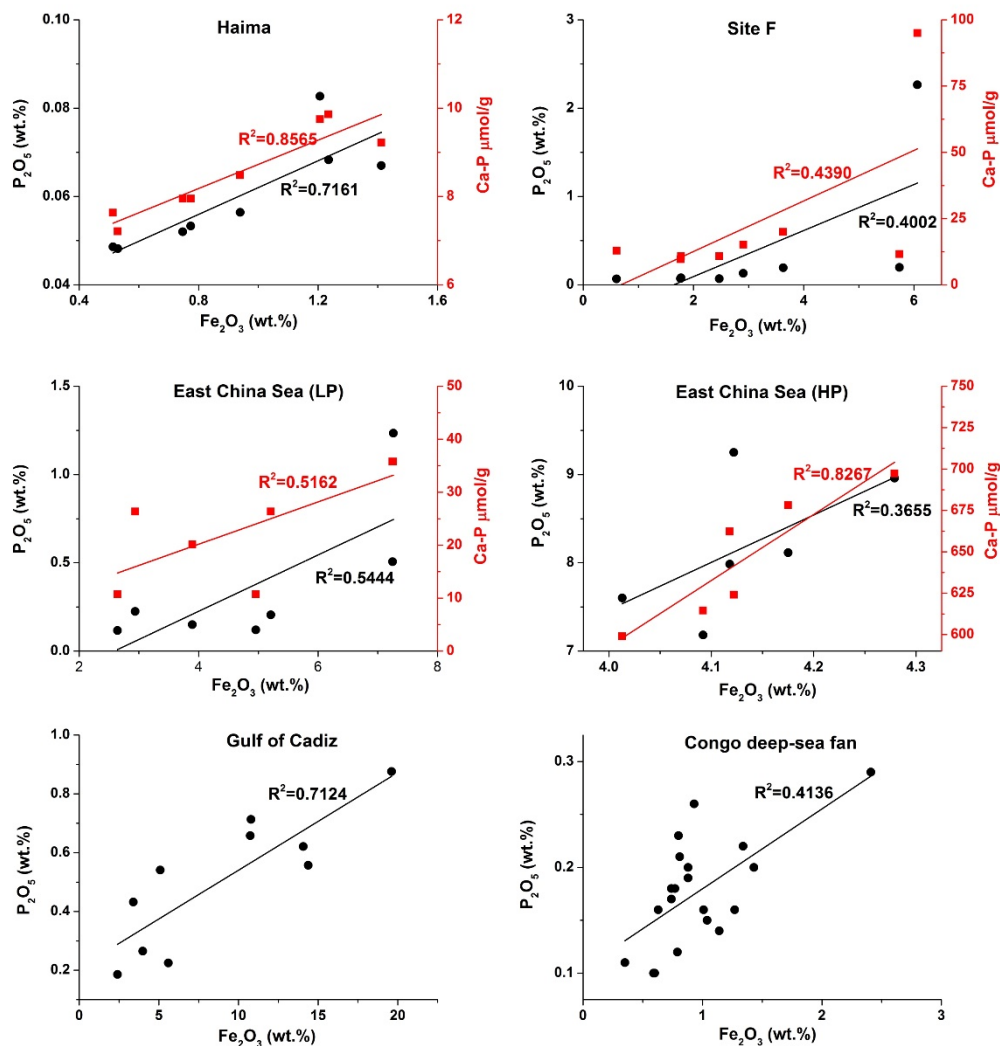


Figure 3. Positive correlations between P_2O_5 (wt.%) and Fe_2O_3 (wt.%), Ca-P ($\mu\text{mol/g}$), and Fe_2O_3 (wt.%) from carbonates in Haima, Site F, and Site E. Positive correlation between P_2O_5 (wt.%) and Fe_2O_3 (wt.%) also found from carbonates in Congo deep-sea fan [7] and Gulf of Cadiz [6].

4.3. Identification of Organic-P in the Carbonates

SEM observations of thin sections and freshly fractured carbonate rocks from Haima, Site F, and Site E reveal the presence of biofilm-like aggregates in the seep carbonates (Figure S4a–c). EDS analyses reveals that they are composed primarily of C and O, indicating that they may be organic matter (Figure S5). Raman spectra collected from each of the aggregates further demonstrate that they are poorly ordered organic matter with a distinct G band ($\sim 1580\text{ cm}^{-1}$) and D band ($\sim 1340\text{ cm}^{-1}$) (Figure S4d, Table S3).

To identify P in the organic matter, 2D Raman mappings and NanoSIMS mapping were performed on an area in the thin section of carbonates from site E (Figure 4). A 2D Raman image, acquired in spectral windows centered on G band of organic matter, reveals the distribution of organic matter in the carbonate deposits (Figure 4b). NanoSIMS images further reveal the distribution of biologically significant elements ($^{12}\text{C}^-$, $^{12}\text{C}^{14}\text{N}^-$, $^{31}\text{P}^-$, and $^{32}\text{S}^-$) within this organic matter (Figure 4d–h). The $^{12}\text{C}^-$, $^{12}\text{C}^{14}\text{N}^-$, and $^{32}\text{S}^-$ maps were similar. $^{31}\text{P}^-$ was also detected to locally accumulate in organic

matter. The overlapped image of $^{31}\text{P}^-$ and $^{32}\text{S}^-$ ion images was consistent with the distribution of $^{12}\text{C}^-$ and $^{12}\text{C}^{14}\text{N}^-$, which represent organic matter (Figure 4i).

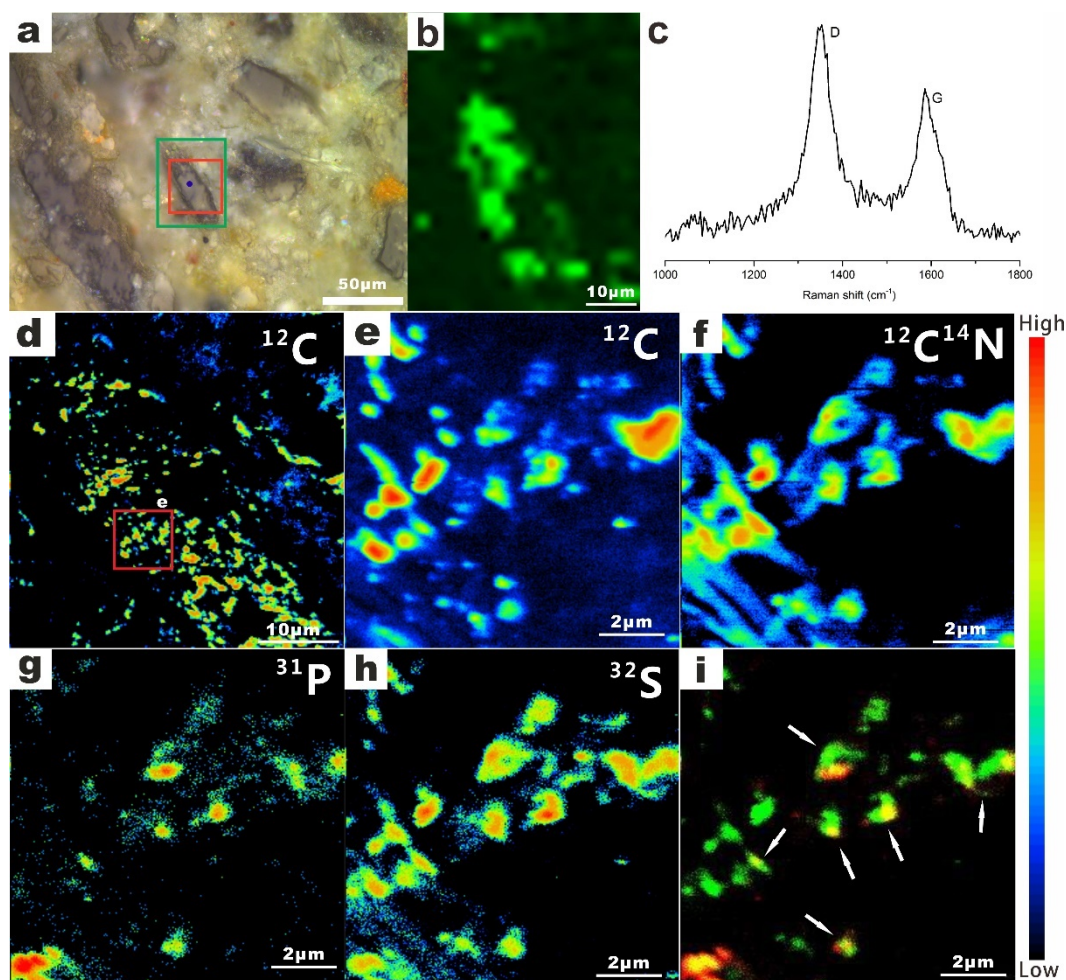


Figure 4. Raman and nanoSIMS elemental mapping of organic matters in carbonates from Site E. (a) Reflected-light photomicrography of thin sections of carbonates. Scale bar = 50 μm . (b) The two-dimensional Raman image showing the distribution of organic matters (G band) (green) in the red box in (a). Scale bar = 5 μm . (c) Raman spectrum acquired from the black spot in (a) showing the D and G band of the organic matter. (d) The $^{12}\text{C}^-$ ion distribution of the organic matter in the green box in (a). Scale bar = 10 μm . (e–h) The $^{12}\text{C}^-$, $^{12}\text{C}^{14}\text{N}^-$, $^{31}\text{P}^-$, and $^{32}\text{S}^-$ ion distribution of the organic matter in red box in (d). Scale bar = 2 μm . (i) Overlapped image of $^{31}\text{P}^-$ (red) and $^{32}\text{S}^-$ (green) ion images. Scale bar = 2 μm .

4.4. Identification of Detrital-P and Authigenic Ca-P in the Carbonates

SEM observations and elemental mapping of thin sections and freshly fractured carbonate rocks reveal the presence of detrital-P in the carbonates from the three cold seeps (Figure 5). EDS analyses reveals that these grains are composed primarily of Ca, P, and O, and may therefore be phosphate minerals (Figure S6). The Raman spectrum at $\sim 965\text{ cm}^{-1}$ provides evidence for the presence of detrital apatite in the samples. The peaks at $\sim 280\text{ cm}^{-1}$ and $\sim 1088\text{ cm}^{-1}$ represent coexisting calcite in the matrix of these samples. The other peaks at $\sim 464\text{ cm}^{-1}$, $\sim 619\text{ cm}^{-1}$, $\sim 970\text{ cm}^{-1}$, and $\sim 1056\text{ cm}^{-1}$ represent monazite, which is another detrital phosphate mineral in the carbonates from Site E (Figure 5g, Table S3).

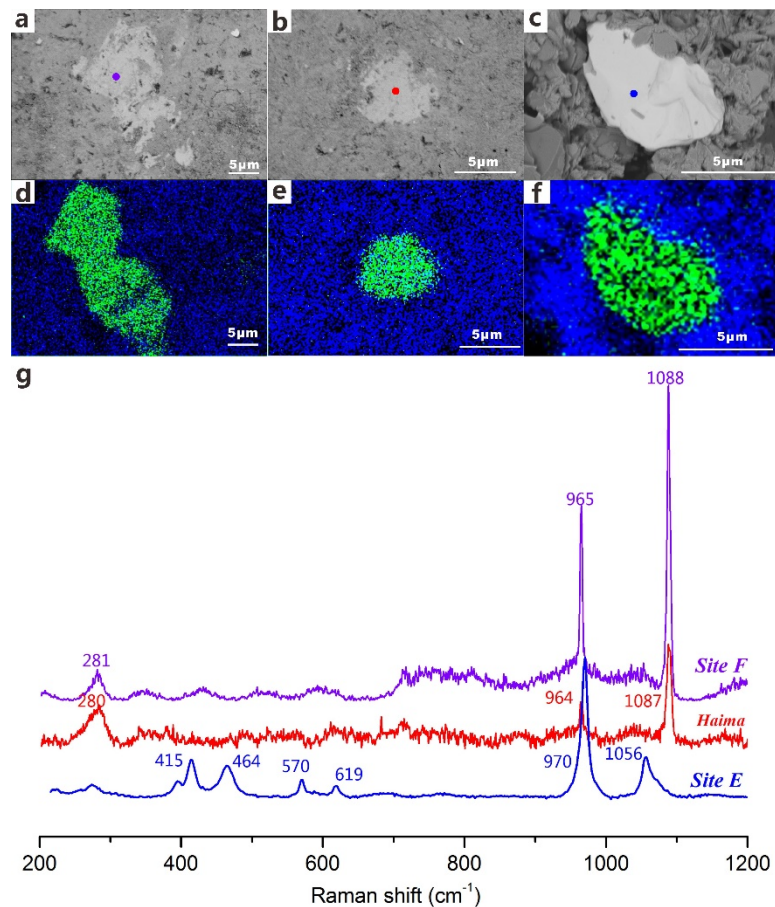


Figure 5. SEM images and elemental mappings of detrital-P in seep carbonates at Site F (a), Haima (b), and Site E (c). Scale bars = 5 μm . (d–f) Elemental images of P in (a), (b), and (c), blue represents Ca distribution and green represents P distribution. Scale bars = 5 μm . (g) Representative Raman spectrums of detrital-P from carbonates in Site F (purple spot in a), Haima (red spot in b), and Site E (blue spot in c). The major band ($\sim 965\text{ cm}^{-1}$) represents phosphate minerals. Bands $\sim 970\text{ cm}^{-1}$ and $\sim 1056\text{ cm}^{-1}$ represent phosphate minerals (monazite). Bands $\sim 1088\text{ cm}^{-1}$ and $\sim 280\text{ cm}^{-1}$ represent carbonate minerals (calcite).

Elemental mapping using NanoSIMS provides further evidence for the presence of P within the Ca-carbonate minerals, indicating that it may be Ca-P (Figure 6). The distributions of $^{12}\text{C}^-$, $^{40}\text{Ca}^{16}\text{O}^-$, and $^{31}\text{P}^-$ are consistent with each other at Site E and Site F, although the intensity of $^{31}\text{P}^-$ in Site E is higher than that from Site F. The $^{12}\text{C}^-$ and $^{40}\text{Ca}^{16}\text{O}^-$ distributions illustrate the matrix, which is composed by Ca-carbonate mineral (calcite) and identified by Raman spectra. The high consistency in the distributions of $^{40}\text{Ca}^{16}\text{O}^-$ and $^{31}\text{P}^-$ (Figure 6e,f) implies that P may be related to the Ca-carbonate mineral (aragonite and calcite).

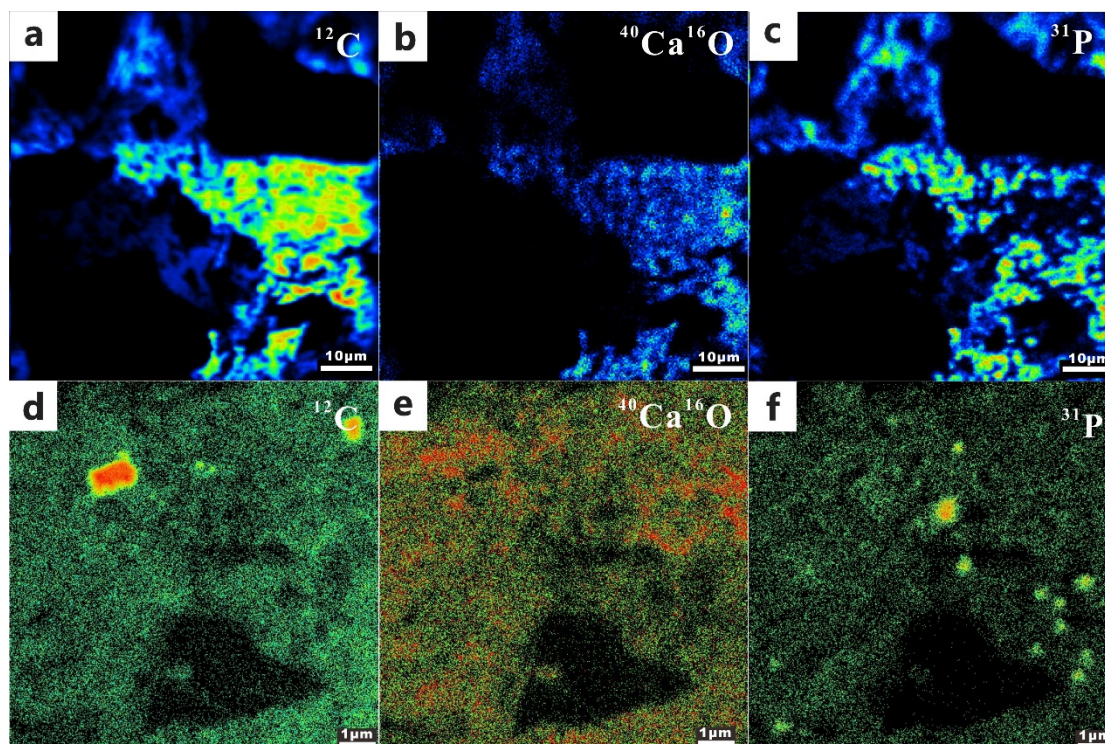


Figure 6. NanoSIMS elemental mapping of authigenic Ca-P in the carbonates. (a–c) The $^{12}\text{C}^-$, $^{40}\text{Ca}^{16}\text{O}^-$, and $^{31}\text{P}^-$ distributions of the carbonate from Site E. Scale bar = 10 μm . (d–f) The $^{12}\text{C}^-$, $^{40}\text{Ca}^{16}\text{O}^-$, and $^{31}\text{P}^-$ distributions of the carbonate from Site F. Scale bar = 1 μm .

5. Discussion

5.1. Distribution of P Species at Cold Seeps

The concentrations of P at the three seep sites differ from each other. The average concentrations of total sedimentary P at Site F and Haima Seep in the northern South China Sea are low. High P concentrations (0.12–9.25 wt.%), however, are evident in the carbonates from Site E. Compared to the northern South China Sea, the East China Sea receives large amounts of sediments from the large rivers of East Asia, including the Yangtze River and the Yellow River, which provide more P at Site E [32,33]. Biogenic sinking particles produced in the water column is another possible source of P [34]. However, the very low concentrations of reactive organic C in the sediments around the seep carbonates at site E suggest that the biogenic source of P may be limited [12].

It has been assumed that authigenic Ca-P accounts for ~50% of all P buried in marine sediments globally [35]. In the present study, authigenic Ca-P also accounts for the largest proportion (21–77%) of sedimentary P in the carbonates at all the three seep sites. Sulfate-driven anaerobic oxidation of methane could cause the precipitation of authigenic Ca-carbonates in the sediments or at the seafloor by increasing the alkalinity in pore water in cold-seep settings [6,16,36]. These Ca carbonates may function as nucleation sites for authigenic Ca-P precipitation [37]. This is consistent with our NanoSIMS results, which reveal similar distribution patterns of ^{12}C , $^{40}\text{Ca}^{16}\text{O}$, and ^{31}P in the carbonates (Figure 5e,f). It suggests that P in cold seep fluid may uptake onto the surface of seep carbonate to form amorphous authigenic Ca-P precursor phases in the sulfate-methane transition zone [38]. It was proposed that the initial uptake of phosphate by Ca carbonate occurs by chemisorption, followed by a gradual transformation of amorphous calcium phosphate to crystalline apatite [39]. While aragonite initially adsorbs more P than calcite and the uptake rate for calcite decreases slowly than that for aragonite [37]. Experimental results also revealed that an increase in temperature and decrease in salinity could increase the equilibrium adsorption of phosphate by calcite and aragonite [40]. Within the sulfate methane

transition zone, which is characterized by a lower salinity and higher alkalinity compared to normal seawater, thermodynamic conditions for authigenic Ca-P formation would be more favorable [38]. Considering that Ca carbonate is the major precipitate in the process of anaerobic oxidation of methane, we postulate that authigenic Ca-P associated with Ca-carbonates plays a key role in P retention in the cold seep environment.

Detrital-P is defined as mineral-bound P (magmatic/metamorphic fluorapatite) that is not bioavailable prior to its deposition at the sea floor and does not undergo phase alterations upon burial [26,41]. It is postulated that the detrital-P fraction is derived from a terrestrial source and can be defined as non-reactive P [41]. The positive correlation between the detrital P and Al_2O_3 (wt.%) contents indicates that the detrital P in the carbonates at the three seep sites originates from terrestrial sediment (Figure 7A). The high concentrations of the detrital-P in the cold-seep carbonates from Site E indicates that this site receives more terrestrial detrital components from the Yangtze River [25].

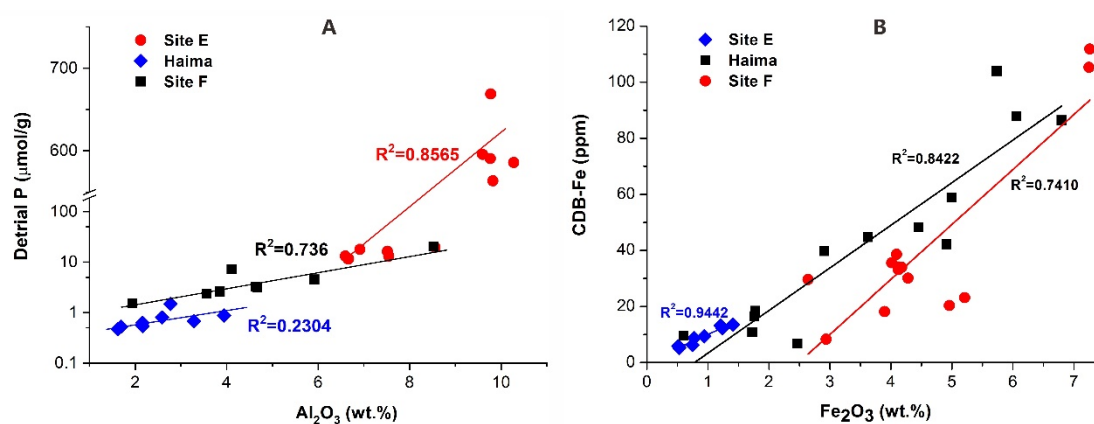


Figure 7. (A) Positive correlations between detrital-P ($\mu\text{mol-P/g}$) and Al_2O_3 (wt.%) from carbonates in Haima, Site F, and Site E. (B) Positive correlations between citrate-dithionite bicarbonate (CDB)-extracted Fe (ppm) and Fe_2O_3 (wt.%) from carbonates in Haima, Site F, and Site E.

Fe-oxides and vivianite-type Fe(II)-P minerals may contribute to the Fe-P content [42,43], which is assumed to account for ~25% of all the P buried in marine sediments [35]. For our study sites, the Fe-P concentrations vary from 1% to 59%. The high correlation between CDB-extracted Fe and total Fe (Figure 7B) indicates that Fe-oxides are the main form in the samples, as CDB-extracted Fe is generally taken to represent total Fe-oxides [44]. The high Fe/P ratio in the CDB extracts also indicate that P binds to the poorly crystalline Fe-oxides rather than forming Fe phosphates such as vivianite [27,45]. This result is consistent with the fact that no vivianite was identified by powder XRD (Figure S2) and SEM-EDS analyses. These techniques are considered effective for identifying vivianite in marine sediments [1]. As the study area in the East China Sea is a non-steady-state depositional system, we infer that the Fe-oxides could be from terrestrial input and rapidly be buried by turbidites at depth [12]. Thus, the Fe-P did not originate from P in seep fluids.

Organic-P is an important carrier of phosphorus to marine sediments and constitutes a large portion of TP (~25%) buried in marine sediments [35]. In this study, organic-P accounted for 1–5% of TP in cold seep carbonates. The most likely source of organic-P in these carbonates is chemolithoautotrophic microorganisms, which are common in cold seep systems. The sulfate-driven anaerobic oxidation of methane that occurs at cold seeps is considered to be mediated by a consortium of methanotrophic archaea and sulfate-reducing bacteria. Both of these could contribute to organic-P compounds such as ATP, DNA, phospholipids, phosphonates, and phosphonic esters in the carbonates [34]. In particular, it has been demonstrated that sulfate reducing bacteria can significantly enrich P in their cells during the process of anaerobic oxidation of methane, although the mechanism for P enrichment in sulfate-reducing bacteria cells is unknown [5]. The distribution pattern of P and S in the organic matter aggregates (Figure 4i) is similar to that in the anaerobic oxidation of methane culture (Figure 2c

in [5]). This suggests that they may represent a consortium of P-rich sulfate-reducing bacteria cells and S-rich anaerobic methanotrophic archaea cells in the carbonates.

The carbonates at the three seep sites had relatively lower exchangeable P, indicating that most of the labile P could probably have been released into the water column.

5.2. Origin and Cycling of P at Cold Seeps

In continental margin environments, the coupled cycling of Fe and P is a dynamic process [13,34,44,46–49]. This is because the P associated with Fe oxides can be liberated during the reduction of Fe-oxides [1]. The positive correlation between Fe and P in the carbonate samples from this study (Site F, Haima, and Site E), the Congo deep-sea fan [7], and Gulf of Cadiz [6] indicates that a coupling relationship also exists between Fe and P in the cold seep settings (Figure 3). Dissolved inorganic P in the seep fluid could be released by the reduction of Fe-oxide coupled with either organic matter oxidation [50,51] or anaerobic oxidation of methane [1,52]. In the former case, the dissimilatory Fe reduction coupled with organic matter oxidation commonly occurs above the sulfate reduction zone in marine sediments [1,50]. However, in cold seep environments, the dissimilatory Fe reduction could be inhibited by the high rate of bacterial sulfate reduction and low reactive organic carbon supply [12,50,51,53,54]. In the latter case, Fe reduction coupled with anaerobic oxidation of methane (namely, Fe-driven anaerobic oxidation of methane) has been identified in different sedimentary environments such as brackish coastal sediments [1,55], basin sediments [53], lake sediments [56], and marine cold seep sediments [12,52,57]. Evidence from porewater geochemistry in the sediment columns shows that Fe-driven anaerobic oxidation of methane occurs in the zone above the deep methanogenic zone and beneath the sulfate-methane transition zone [53]. This is distinctly different from the zoning in marine sediments, where the iron reduction zone is commonly above the sulfate reduction zone [1,53]. Sulfur driven Fe release and deep cryptic S cycling may also result in the release of ferrous iron into solution [58,59]. However, Fe isotope and sulfur isotope composition of pyrites in Site E [12] suggested that Fe reduction coupled with anaerobic oxidation of methane might occur in the study area. Thus, we propose that Fe reduction is coupled to anaerobic oxidation of methane liberates P associated with Fe oxides below the sulfate-methane transition zone and ultimately results in the accumulation of P in the cold seep fluid in the study areas.

While the formation of authigenic Ca-P is a widespread phenomenon in marine sediments, the exact mechanism is still not clear. Sink switching, transfer of P from labile forms into authigenic Ca-P, is thought to be the predominant process leading to the burial of P in marine deposits worldwide [27,60,61]. Recently, it has been suggested that authigenic Ca-P precipitation may take place at the sulfate-methane transition zones in continental margin sediments and that authigenic Ca-P precipitation below sulfate–methane transition zone probably does not take place [38,47].

It has demonstrated that it is a simultaneous phase of two anaerobic oxidation of methane processes in and around sulfate–methane transition zone from seep carbonates in the East China Sea [12,22,62]. In the sulfate–methane transition zone, sulfate-driven anaerobic oxidation of methane processes results in increased alkalinity levels in the pore waters that lead to precipitation of carbonates in and around the seep fluid conduits [6,16,36]. P in the cold seep fluid originates from below the sulfate–methane transition zone and is adsorbed by chemisorption within Ca-carbonate minerals [37,39,40], which is shown by the NanoSIMS ion mapping in our samples. That is to say, the authigenic Ca-P is enriched in the seep carbonates that are considered to form in the sulfate-methane transition zone.

5.3. A Potential Model for P Cycling in Cold Seep Environments

We postulate that the P in the cold seep fluid is derived mainly from the liberation of P from Fe-oxides in the process of Fe-driven anaerobic oxidation of methane that occurs in the deep, anoxic sediments. The abundant Fe oxides derived from terrestrial input can function as electron acceptors for the biological oxidation of CH₄ released from the sub-seafloor gas hydrate reservoir. In the absence of Fe-driven anaerobic oxidation of methane that occur below the sulfate-methane transition zone, most

of the Fe-oxide bound P at depth would be retained in the sediments. The cold seep fluids containing dissolved P migrate upward and result in the co-precipitation of Ca-P with Ca-carbonates, which are formed during the sulfate-driven anaerobic oxidation of methane in the sulfate–methane transition zone. The presence of hydrogen sulfate and sulfide in the sulfate–methane transition zone, however, is favorable to the formation of pyrite rather than Fe phosphates such as vivianite [38]. Therefore, Ca-P is dominant in all the carbonates rather than Fe phosphate. During the sulfate-driven anaerobic oxidation of methane, a small portion of P in the fluids could be utilized by chemolithoautotrophic microorganisms (e.g., methanotrophic archaea and sulfate-reducing bacteria) and preserved as cellular organic-P in the carbonates. Apart from the P species deposited in the carbonates, a part of the P in the cold seep fluid may be discharged directly at the seafloor and be used by the cold seep biota. The amounts, however, remain unknown and should be quantified.

6. Conclusions

In seep carbonates, Ca-P accounts for the largest proportion, followed by detrital-P, Fe-P, exchangeable-P, and organic-P. The partition of P species in the carbonates illustrates that a large portion of the P in the fluids precipitate in the form of Ca-P within Ca-carbonate minerals associated with sulfate-driven anaerobic oxidation of methane. Although chemolithoautotrophic microorganisms involved in the anaerobic oxidation of methane may contribute organic-P to the carbonates, the amount of organic-P is a marginal fraction of the total sedimentary P (1–7%). The positive correlation between the Ca-P and Fe contents indicates that the dissolved P in the fluids is primarily released from Fe-oxides through Fe reduction coupled with Fe-driven anaerobic oxidation of methane, in deep sediments. A model of the P cycle in deep-sea cold seep environments is proposed in the present study. We postulate that similar geochemical processes may occur widely in global cold seep systems, as indicated by the positive correlation between the P and Fe concentration observed in seep carbonates from Congo deep-sea fan [7] and Gulf of Cadiz [6]. Our results are helpful to better understand deep sea P biogeochemical cycling and anaerobic oxidation of methane at cold seep environments.

Supplementary Materials: The following files are available online at <http://www.mdpi.com/2075-163X/10/7/645/s1>, Figure S1: Authigenic carbonate samples from Site E (A), Haima (B), and Site F (C). Figure S2: XRD spectra showing the mineral composition of the carbonates from three seep sites. Figure S3: Positive linear relation ($R^2 = 0.9848$) between P_2O_5 (wt.%) determined by XRF and total phosphorus extracted by sequential extraction method of all the carbonates from three seep sites. Figure S4: SEM images of organic matters and their corresponding Raman spectra from seep carbonates. Figure S5: SEM-EDS analysis of organic matters from Site F (Figure S4a), Haima (Figure S4b), and Site E (Figure S4c). Figure S6: SEM-EDS analysis of detrital-P from Site F (Figure 6b), Haima (Figure 6c), and Site E (Figure 6d). Table S1: Chemical compositions of the seep carbonates at Haima, Site F, and Site E. Table S2: The concentrations of each P species, total inorganic P and total sedimentary P in the seep carbonates at Site E, Haima, and Site F. Table S3: Main Raman vibrations (cm^{-1}) of organic matters and minerals in the seep carbonates.

Author Contributions: Conceptualization, J.Z. and X.P.; formal analysis, J.Z.; funding acquisition, X.P.; investigation, J.Z., X.P., J.L., H.X., K.T., S.C., and M.D.; methodology, J.Z. and J.L.; project administration, X.P.; resources, X.P. and K.T.; supervision, X.P.; visualization, J.Z.; writing—original draft, J.Z.; writing—review and editing, J.Z., X.P., J.L., H.X., K.T., S.C., and M.D. All authors have read and agreed to the published version of the manuscript.

Funding: This study was financially supported by the National Key Research and Development Program of China (Grant No. 2017YFC0306702 and 2016YFC0304900).

Acknowledgments: We are thankful to the crews of the R/V *Tan Suo Yi Hao* and *KexueYihao* for their help during the Expeditions. We are deeply indebted to Brian Jones at University of Alberta for his editing and constructive suggestions to this paper.

Conflicts of Interest: The authors declare that they have no conflicts of interest regarding the publication of this paper.

References

1. Egger, M.; Jilbert, T.; Behrends, T.; Rivard, C.; Slomp, C.P. Vivianite is a major sink for phosphorus in methanogenic coastal surface sediments. *Geochim. Cosmochim. Acta* **2015**, *169*, 217–235. [[CrossRef](#)]
2. Kraal, P.; Dijkstra, N.; Behrends, T.; Slomp, C.P. Phosphorus burial in sediments of the sulfidic deep Black Sea: Key roles for adsorption by calcium carbonate and apatite authigenesis. *Geochim. Cosmochim. Acta* **2017**, *204*, 140–158. [[CrossRef](#)]
3. Feng, D.; Qiu, J.W.; Hu, Y.; Peckmann, J.; Guan, H.X.; Tong, H.P.; Chen, C.; Chen, J.X.; Gong, S.G.; Li, N.; et al. Cold seep systems in the South China Sea: An overview. *J. Asian Earth Sci.* **2018**, *168*, 3–16. [[CrossRef](#)]
4. Boetius, A.; Ravensschlag, K.; Schubert, C.J.; Rickert, D.; Widdel, F.; Gieseke, A.; Amann, R.; Jørgensen, B.B.; Witte, U.; Pfannkuche, O. A marine microbial consortium apparently mediating anaerobic oxidation of methane. *Nature* **2000**, *407*, 623–626. [[CrossRef](#)] [[PubMed](#)]
5. Milucka, J.; Ferdelman, T.G.; Polerecky, L.; Franzke, D.; Wegener, G.; Schmid, M.; Lieberwirth, I.; Wagner, M.; Widdel, F.; Kuypers, M.M. Zero-valent sulphur is a key intermediate in marine methane oxidation. *Nature* **2012**, *491*, 541–546. [[CrossRef](#)]
6. Diaz-del-Rio, V.; Somoza, L.; Martinez-Frias, J.; Mata, M.P.; Delgado, A.; Hernandez-Molina, F.J.; Lunar, R.; Martin-Rubi, J.A.; Maestro, A.; Fernandez-Puga, M.C.; et al. Vast fields of hydrocarbon-derived carbonate chimneys related to the accretionary wedge/olistostrome of the Gulf of Cádiz. *Mar. Geol.* **2003**, *195*, 177–200. [[CrossRef](#)]
7. Pierre, C.; Fouquet, Y. Authigenic carbonates from methane seeps of the Congo deep-sea fan. *Geo-Mar. Lett.* **2007**, *27*, 249–257. [[CrossRef](#)]
8. Pierre, C.; Bayon, G.; Blanc-Valleron, M.M.; Mascle, J.; Dupré, S. Authigenic carbonates related to active seepage of methane-rich hot brines at the Cheops mud volcano, Menes caldera (Nile deep-sea fan, eastern Mediterranean Sea). *Geo-Mar. Lett.* **2014**, *34*, 253–267. [[CrossRef](#)]
9. Ruffine, L.; Caprais, J.-C.; Bayon, G.; Riboulot, V.; Donval, J.-P.; Etoubleau, J.; Birot, D.; Pignet, P.; Rongemaille, E.; Chazallon, B.; et al. Investigation on the geochemical dynamics of a hydrate-bearing pockmark in the Niger Delta. *Mar. Pet. Geol.* **2013**, *43*, 297–309. [[CrossRef](#)]
10. Viola, I.; Oppo, D.; Franchi, F.; Capozzi, R.; Dinelli, E.; Liverani, B.; Taviani, M. Mineralogy, geochemistry and petrography of methane-derived authigenic carbonates from Enza River, Northern Apennines (Italy). *Mar. Pet. Geol.* **2015**, *66*, 566–581. [[CrossRef](#)]
11. Viola, I.; Capozzi, R.; Bernasconi, S.M.; Rickli, J. Carbon, oxygen and strontium isotopic constraints on fluid sources, temperatures and biogeochemical processes during the formation of seep carbonates—Secchia River site, Northern Apennines. *Sediment. Geol.* **2017**, *357*, 1–15. [[CrossRef](#)]
12. Peng, X.; Guo, Z.; Chen, S.; Sun, Z.; Xu, H.; Ta, K.; Zhang, J.; Zhang, L.; Li, J.; Du, M. Formation of carbonate pipes in the northern Okinawa Trough linked to strong sulfate exhaustion and iron supply. *Geochim. Cosmochim. Acta* **2017**, *205*, 1–13. [[CrossRef](#)]
13. Egger, M.; Hagens, M.; Sapart, C.J.; Dijkstra, N.; Van Helmond, N.A.G.M.; Mogollón, J.M.; Risgaard-Petersen, N.; Van Der Veen, C.; Kasten, S.; Riedinger, N.; et al. Iron oxide reduction in methane-rich deep Baltic Sea sediments. *Geochim. Cosmochim. Acta* **2017**, *207*, 256–276. [[CrossRef](#)]
14. Feng, D.; Chen, D.F. Authigenic carbonates from an active cold seep of the northern South China Sea: New insights into fluid sources and past seepage activity. *Deep Sea Res. Part II Top. Stud. Oceanogr.* **2015**, *122*, 74–83. [[CrossRef](#)]
15. Lin, Z.; Sun, X.; Peckmann, J.; Lu, Y.; Xu, L.; Strauss, H.; Zhou, H.; Gong, J.; Lu, H.; Teichert, B.M.A. How sulfate-driven anaerobic oxidation of methane affects the sulfur isotopic composition of pyrite: A SIMS study from the South China Sea. *Chem. Geol.* **2016**, *440*, 26–41. [[CrossRef](#)]
16. Peckmann, J.; Reimer, A.; Luth, U.; Luth, C.; Hansen, B.T.; Heinicke, C.; Hoefs, J.; Reitner, J. Methane-derived carbonates and authigenic pyrite from the northwestern Black Sea. *Mar. Geol.* **2001**, *177*, 129–150. [[CrossRef](#)]
17. Peckmann, J.; Birgel, D.; Kiel, S. Molecular fossils reveal fluid composition and flow intensity at a Cretaceous seep. *Geology* **2009**, *37*, 847–850. [[CrossRef](#)]
18. Peckmann, J.; Thiel, V. Carbon cycling at ancient methane-seeps. *Chem. Geol.* **2004**, *205*, 443–467. [[CrossRef](#)]
19. Feng, D.; Peng, Y.; Bao, H.; Peckmann, J.; Roberts, H.H.; Chen, D. A carbonate-based proxy for sulfate-driven anaerobic oxidation of methane. *Geology* **2016**, *44*, 999–1002. [[CrossRef](#)]

20. Liang, Q.; Hu, Y.; Feng, D.; Peckmann, J.; Chen, L.; Yang, S.; Liang, J.; Tao, J.; Chen, D. Authigenic carbonates from newly discovered active cold seeps on the northwestern slope of the South China Sea: Constraints on fluid sources, formation environments, and seepage dynamics. *Deep Sea Res. Part I Oceanogr. Res. Pap.* **2017**, *124*, 31–41. [[CrossRef](#)]
21. Liu, C.S.; Morita, S.; Liao, Y.H.; Ku, C.K.; Machiyama, H.; Lin, S.; Soh, W. High-resolution seismic images of the formosa ridge off southwestern taiwan where “hydrothermal” chemosynthetic community is present at a cold seep site. In Proceedings of the 6th International Conference on Gas Hydrates, Vancouver, BC, Canada, 6–10 July 2008.
22. Li, J.; Peng, X.; Bai, S.; Chen, Z.; Van Nostrand, J.D. Biogeochemical processes controlling authigenic carbonate formation within the sediment column from the Okinawa Trough. *Geochim. Cosmochim. Acta* **2018**, *222*, 363–382. [[CrossRef](#)]
23. Sun, Z.; Wei, H.; Zhang, X.; Shang, L.; Yin, X.; Sun, Y.; Xu, L.; Huang, W.; Zhang, X. A unique Fe-rich carbonate chimney associated with cold seeps in the Northern Okinawa Trough, East China Sea. *Deep Sea Res. Part I Oceanogr. Res. Pap.* **2015**, *95*, 37–53. [[CrossRef](#)]
24. Sibuet, M.; Olu, K. Biogeography, biodiversity and fluid dependence of deep-sea cold-seep communities at active and passive margins. *Deep Sea Res. Part II Top. Stud. Oceanogr.* **1998**, *45*, 517–567. [[CrossRef](#)]
25. Wu, Z.; Li, J.; Jin, X.; Shang, J.; Li, S.; Jin, X. Distribution, features, and influence factors of the submarine topographic boundaries of the Okinawa Trough. *Sci. China Earth Sci.* **2014**, *57*, 1885–1896. [[CrossRef](#)]
26. Ruttenger, K.C. Development of a sequential extraction method for different forms of phosphorus in marine-sediments. *Limnol. Oceanogr.* **1992**, *37*, 1460–1482. [[CrossRef](#)]
27. Slomp, C.P.; Epping, E.H.G.; Helder, W.; Van Raaphorst, W. A key role for iron-bound phosphorus in authigenic apatite formation in North Atlantic continental platform sediments. *J. Mar. Res.* **1996**, *54*, 1179–1205. [[CrossRef](#)]
28. Kraal, P.; Slomp, C.P.; Forster, A.; Kuypers, M.M.M.; Sluijs, A. Pyrite oxidation during sample storage determines phosphorus fractionation in carbonate-poor anoxic sediments. *Geochim. Cosmochim. Acta* **2009**, *73*, 3277–3290. [[CrossRef](#)]
29. Murphy, J.; Riley, J.P. A Single-Solution Method for the Determination of Soluble Phosphate in Sea Water. *J. Mar. Biol. Assoc. UK* **1958**, *37*, 9–14. [[CrossRef](#)]
30. Ammar, M.R.; Rouzaud, J.N. How to obtain a reliable structural characterization of polished graphitized carbons by Raman microspectroscopy. *J. Raman Spectrosc.* **2012**, *43*, 207–211. [[CrossRef](#)]
31. Peng, X.; Guo, Z.; House, C.H.; Chen, S.; Ta, K. SIMS and NanoSIMS analyses of well-preserved microfossils imply oxygen-producing photosynthesis in the Mesoproterozoic anoxic ocean. *Chem. Geol.* **2016**, *441*, 24–34. [[CrossRef](#)]
32. Katayama, H.; Watanabe, Y. The Huanghe and Changjiang contribution to seasonal variability in terrigenous particulate load to the Okinawa Trough. *Deep Sea Res. Part II Top. Stud. Oceanogr.* **2003**, *50*, 475–485. [[CrossRef](#)]
33. Sibuet, J.C.; Letouzey, J.; Barbier, F.; Charvet, J.; Foucher, J.-P.; Hilde, T.W.C.; Kimura, M.; Chiao, L.-Y.; Marsset, B.; Muller, C.; et al. Back Arc Extension in the Okinawa Trough. *J. Geophys. Res. Sol. Ea.* **1987**, *92*, 14041–14063. [[CrossRef](#)]
34. Ruttenger, K.C. The global phosphorus cycle. In *Treatise on Geochemistry*; Holland, H.D., Turekian, K.K., Eds.; Elsevier: Amsterdam, The Netherlands, 2014; Volume 10, pp. 499–558.
35. Ruttenger, K.C. The global phosphorus cycle. In *Treatise on Geochemistry*; Turekian, K.K., Holland, D.J., Eds.; Elsevier: Amsterdam, The Netherlands, 2003; pp. 585–643.
36. Bayon, G.; Dupré, S.; Ponzevera, E.; Etoubleau, J.; Chéron, S.; Pierre, C.; Mascle, J.; Boetius, A.; De Lange, G.J. Formation of carbonate chimneys in the Mediterranean Sea linked to deep-water oxygen depletion. *Nat. Geosci.* **2013**, *6*, 755. [[CrossRef](#)]
37. De Kanel, J.; Morse, J.W. The chemistry of orthophosphate uptake from seawater on to calcite and aragonite. *Geochim. Cosmochim. Acta* **1978**, *42*, 1335–1340. [[CrossRef](#)]
38. März, C.; Riedinger, N.; Sena, C.; Kasten, S. Phosphorus dynamics around the sulphate-methane transition in continental margin sediments: Authigenic apatite and Fe(II) phosphates. *Mar. Geol.* **2018**, *404*, 84–96. [[CrossRef](#)]
39. Stumm, W.; Leckie, J.O. Phosphate exchange with sediments: Its role in the productivity of surface waters. *Advan. Water Pollut. Res.* **1971**, *5*, 1–26.

40. Millero, F.; Huang, F.; Zhu, X.; Liu, X.; Zhang, J.Z. Adsorption and Desorption of Phosphate on Calcite and Aragonite in Seawater. *Aquat. Geochem.* **2001**, *7*, 33–56. [[CrossRef](#)]
41. März, C.; Poulton, S.W.; Wagner, T.; Schnetger, B.; Brumsack, H.J. Phosphorus burial and diagenesis in the central Bering Sea (Bowers Ridge, IODP Site U1341): Perspectives on the marine P cycle. *Chem. Geol.* **2014**, *363*, 270–282. [[CrossRef](#)]
42. Dijkstra, N.; Kraal, P.; Kuypers, M.M.; Schnetger, B.; Slomp, C.P. Are iron-phosphate minerals a sink for phosphorus in anoxic Black Sea sediments? *PLoS ONE* **2014**, *9*, e101139. [[CrossRef](#)]
43. Nembrini, G.P.; Capobianco, J.A.; Viel, M.; Williams, A.F. A Mössbauer and chemical study of the formation of vivianite in sediments of Lago Maggiore (Italy). *Geochim. Cosmochim. Acta* **1983**, *47*, 1459–1464. [[CrossRef](#)]
44. Slomp, C.P.; Mort, H.P.; Jilbert, T.; Reed, D.C.; Gustafsson, B.G.; Wolthers, M. Coupled dynamics of iron and phosphorus in sediments of an oligotrophic coastal basin and the impact of anaerobic oxidation of methane. *PLoS ONE* **2013**, *8*, e62386. [[CrossRef](#)] [[PubMed](#)]
45. Dellwig, O.; Leipe, T.; März, C.; Glockzin, M.; Pollehne, F.; Schnetger, B.; Yakushev, E.V.; Böttcher, M.E.; Brumsack, H.-J. A new particulate Mn–Fe–P-shuttle at the redoxcline of anoxic basins. *Geochim. Cosmochim. Acta* **2010**, *74*, 7100–7115. [[CrossRef](#)]
46. Berner, R.A.; Rao, J.L. Phosphorus in sediments of the Amazon River and estuary: Implications for the global flux of phosphorus to the sea. *Geochim. Cosmochim. Acta* **1994**, *58*, 2333–2339. [[CrossRef](#)]
47. Egger, M.; Kraal, P.; Jilbert, T.; Sulu-Gambari, F.; Sapart, C.J.; Röckmann, T.; Slomp, C.P. Anaerobic oxidation of methane alters sediment records of sulfur, iron and phosphorus in the Black Sea. *Biogeosciences* **2016**, *13*, 5333–5355. [[CrossRef](#)]
48. Jilbert, T.; Slomp, C.P. Iron and manganese shuttles control the formation of authigenic phosphorus minerals in the euxinic basins of the Baltic Sea. *Geochim. Cosmochim. Acta* **2013**, *107*, 155–169. [[CrossRef](#)]
49. Kraal, P.; Burton, E.D.; Rose, A.L.; Kocar, B.D.; Lockhart, R.S.; Grice, K.; Bush, R.T.; Tan, E.; Webb, S.M. Sedimentary iron–phosphorus cycling under contrasting redox conditions in a eutrophic estuary. *Chem. Geol.* **2015**, *392*, 19–31. [[CrossRef](#)]
50. Lovley, D.R.; Phillips, E.J. Competitive mechanisms for inhibition of sulfate reduction and methane production in the zone of ferric iron reduction in sediments. *Appl. Environ. Microbiol.* **1987**, *53*, 2636–2641. [[CrossRef](#)]
51. Johnson, C.M.; Beard, B.L.; Roden, E.E. The Iron Isotope Fingerprints of Redox and Biogeochemical Cycling in Modern and Ancient Earth. *Annu. Rev. Earth Pl. Sci.* **2008**, *36*, 457–493. [[CrossRef](#)]
52. Liu, J.; Izon, G.; Wang, J.; Antler, G.; Wang, Z.; Zhao, J.; Egger, M. Vivianite formation in methane-rich deep-sea sediments from the South China Sea. *Biogeosciences* **2018**, *15*, 6329–6348. [[CrossRef](#)]
53. Riedinger, N.; Formolo, M.J.; Lyons, T.W.; Henkel, S.; Beck, A.; Kasten, S. An inorganic geochemical argument for coupled anaerobic oxidation of methane and iron reduction in marine sediments. *Geobiology* **2014**, *12*, 172–181. [[CrossRef](#)]
54. Sivan, O.; Adler, M.; Pearson, A.; Gelman, F.; Bar-Or, I.; John, S.G.; Eckert, W. Geochemical evidence for iron-mediated anaerobic oxidation of methane. *Limnol. Oceanogr.* **2011**, *56*, 1536–1544. [[CrossRef](#)]
55. Segarra, K.E.A.; Comerford, C.; Slaughter, J.; Joye, S.B. Impact of electron acceptor availability on the anaerobic oxidation of methane in coastal freshwater and brackish wetland sediments. *Geochim. Cosmochim. Acta* **2013**, *115*, 15–30. [[CrossRef](#)]
56. Sivan, O.; Antler, G.; Turchyn, A.V.; Marlow, J.J.; Orphan, V.J. Iron oxides stimulate sulfate-driven anaerobic methane oxidation in seeps. *Proc. Natl. Acad. Sci. USA* **2014**, *111*, E4139–E4147. [[CrossRef](#)] [[PubMed](#)]
57. Beal, E.J.; House, C.H.; Orphan, V.J. Manganese- and iron-dependent marine methane oxidation. *Science* **2009**, *325*, 184–187. [[CrossRef](#)]
58. Holmkvist, L.; Ferdelman, T.G.; Jorgensen, B.B. A cryptic sulfur cycle driven by iron in the methane zone of marine sediment (Aarhus Bay, Denmark). *Geochim. Cosmochim. Acta* **2011**, *75*, 3581–3599. [[CrossRef](#)]
59. Lichtschlag, A.; Kamyshny, A.; Ferdelman, T.G.; DeBeer, D. Intermediate sulfur oxidation state compounds in the euxinic surface sediments of the Dvurechenskii mud volcano (Black Sea). *Geochim. Cosmochim. Acta* **2013**, *105*, 130–145. [[CrossRef](#)]
60. Filippelli, G.M. The global phosphorus cycle: Past, present, and future. *Elements* **2008**, *4*, 89–95. [[CrossRef](#)]

61. Ruttenger, K.C.; Berner, R.A. Authigenic apatite formation and burial in sediments from non-upwelling, continental-margin environments. *Geochim. Cosmochim. Acta* **1993**, *57*, 991–1007. [[CrossRef](#)]
62. Sun, Z.; Wu, N.; Cao, H.; Xu, C.; Liu, L.; Yin, X.; Zhang, X.R.; Geng, W.; Zhang, X.L. Hydrothermal metal supplies enhance the benthic methane filter in oceans: An example from the okinawa trough. *Chem. Geol.* **2019**, *525*, 190–209. [[CrossRef](#)]



© 2020 by the authors. Licensee MDPI, Basel, Switzerland. This article is an open access article distributed under the terms and conditions of the Creative Commons Attribution (CC BY) license (<http://creativecommons.org/licenses/by/4.0/>).